Available online at www.sciencedirect.com
ScienceDirect
Trans. Nonferrous Met. Soc. China 34(2024) 2849−2863
Transactions of Nonferrous Metals Society of China
www.tnmsc.cn

A new rhombohedral phase and its 48 variants in β titanium alloy

Xin-nan WANG[1], Ming HAN[2], Fu-rong ZHANG[2], Guang-ming ZHAO[2], Zhi-shou ZHU[1]

1. Aviation Key Laboratory of Science and Technology on Advanced Titanium Alloys, AECC Beijing Institute of Aeronautical Materials, Beijing 100095, China;
2. School of Materials Science and Engineering, East China Jiaotong University, Nanchang 330013, China

Received 15 March 2023; accepted 28 January 2024

Abstract: A new rhombohedral phase (termed R') in a solution−aging-treated titanium alloy (Ti−4.5Al−6.5Mo−2Cr−2Nb−1V−1Sn−1Zr, wt.%) was identified. Its accurate Bravais lattice parameters were determined by a novel unit cell reconstruction method based on conventional selected-area electron diffraction (SAED) technique. The orientation relationship between R' phase and BCC phase was revealed. The results show that the R' phase is found to have 48 crystallographically equivalent variants, resulting in rather complicated SAED patterns with high-order reflections. A series of in-situ SAED patterns were taken along both low- and high-index zone axes, and all weak and strong reflections arising from the 48 variants were properly explained and directly assigned with self-consistent Miller indices, confirming the presence of the rhombohedral phase. Additionally, some criteria were also proposed for evaluating the indexed results, which together with the Bravais lattice reconstruction method shed light on the microstructure characterization of even unknown phases in other alloys.

Key words: titanium alloy; rhombohedral phase; Bravais lattice reconstruction; variant; orientation relationship

1 Introduction

The physical, chemical, and mechanical properties of solution−aging-treated titanium alloys, crucial in aerospace, marine, medicine, and other practical applications [1−3], are significantly influenced by intermediate phases. These alloys, originating from an oversaturated disordered β [4,5] or ordered β_0 [6] parent phase, undergo diverse phase transformations [7−9] during aging treatment. These transformations yield a series of metastable intermediate phases, including hexagonal structured disordered ω [10], ordered ω'', or ω_0 [11] phases, as well as orthorhombic structured disordered O' [12,13] or ordered O'' [14] phases. Ultimately, the sequence progresses to the stable hexagonal disordered α [15,16] or ordered α_2 [17] phase.

Transmission electron microscopy (TEM) offers exceptional spatial resolution at the atomic level, advantageous for characterizing various intermediate phases. Yet, employing conventional selected-area electron diffraction (SAED) technique in TEM presents formidable challenges in correctly indexing the SAED patterns of fine precipitates. These challenges arise from several factors: (1) Precipitates often form at habit planes in the parent phase, possessing multiple crystallographic variants. Each variant contributes to the SAED pattern, complicating its analysis. (2) SAED patterns of fine intermediate phases usually comprise superimposed single-crystal patterns, making direct indexing for individual reflections overly complex. (3) Acquiring a series of in situ SAED patterns from

Corresponding author: Zhi-shou ZHU, Tel: +86-13501067682, E-mail: zhuzzs@126.com;
Ming HAN, E-mail: mhancn@yahoo.com
DOI: 10.1016/S1003-6326(24)66580-5

a single fine precipitate poses a persistent challenge. (4) Specimen tilting in TEM alters the camera length for different SAED patterns, introducing errors that hinder pattern indexing. (5) Chemical composition non- uniformity can result in incomplete extinction of reflections from ordered structures. (6) The intersection between relrods [18] and the Ewald sphere generates discrete diffraction spots in SAED patterns, even with relrods sharing the same reciprocal lattice point. (7) High-order reflections add complexity to the indexing process, making it challenging to distinguish characteristic parallelograms of different variants. (8) Electron beam illumination may potentially damage the structure of fine precipitates.

Due to the aforementioned challenges, researchers commonly adopt different methods in analyzing SAED patterns for precipitate characterization. One approach involves utilizing simplified SAED patterns along specific low-index zone axes of precipitates. Here, researchers indirectly analyze weak reflections by gauging fractional positions, e.g., 1/2 or 1/3 [19−21] relative to the parent reflections for phase identification, avoiding direct assignment of indices based on precipitate lattice parameters. A more comprehensive method entails a systematic analysis of SAED patterns, where researchers assign indices to all weak and strong reflections from the precipitates. This thorough analysis yields crucial crystallographic information pivotal for comprehending and regulating the roles of these precipitates in enhancing the overall performance of the alloys.

In this study, we introduce a novel method aimed at accurately reconstructing the Bravais lattice of an unknown phase using SAED technique. The focus is on identifying a new rhombohedral phase in an aging-treated titanium alloy. Leveraging the intrinsic crystallographic relationship between the precipitate and the parent phase helps mitigate the impact of measurement errors during the unit cell reconstruction process. The newly discovered rhombohedral phase, denoted as R', exhibits a complex structure with 48 variants, leading to intricate SAED patterns that include high-order reflections. To navigate this complexity, we utilize the reconstructed lattice parameters of the R' phase and its orientation relationship (OR) with the parent. Through a systematic analysis of a series of in situ SAED patterns obtained along both low- and high-index zone axes, we successfully explain and directly assign all weak and strong reflections from the 48 variants, encompassing even high-order reflections. Furthermore, the study delves into criteria for evaluating the indexed results, providing a comprehensive understanding of the precision and reliability of the reconstructed lattice parameters and orientation relationships in the context of the R' phase in the aging-treated titanium alloy.

2 Methodology

2.1 Reconstructing Bravais lattice of precipitate

Theoretically, reconstructing the Bravais lattice of a crystal follows a structured three-step process: Initially, by observing the periodic arrangement of reciprocal lattice planes (RLPs) in 3D space, a primitive unit cell, i.e. an arrangement that describes the reciprocal lattice points, is reconstructed. This primitive cell is delineated by only three RLPs from the same crystal and their respective interplanar angles. Subsequently, the reconstructed 3D primitive cell is simplified to form a Niggli cell. This Niggli cell is defined by the three shortest non-coplanar reciprocal lattice vectors (RLVs). Given that there exist 44 types of Niggli cells and 14 types of Bravais lattices, with an explicit correspondence between the two, the determination of a Bravais cell in reciprocal space becomes feasible. This Bravais cell is then transformed into a real space, ultimately enabling the determination of the Bravais lattice type and its corresponding parameters.

However, practical execution of these steps poses significant challenges, particularly with the first two procedures. The angle (δ) between RLPs can be calculated by the readings of double-tilt holder:

$$\cos\delta=\cos\left(A_2-A_1\right)\cdot\cos\left(B_2-B_1\right)+2\sin A_1\cdot\sin A_2\cdot\sin^2\left(\frac{B_2-B_1}{2}\right) \tag{1}$$

where A and B are the angles of specimen tilting about the two axes (e.g., X and Y) of a double-tilt holder, and the subscripts "1" and "2" represent two states before and after tilting, respectively. Regrettably, the accuracy of angles calculated using Eq. (1) is compromised due to the difficulty in precisely obtaining on-zone SAED patterns. The inherent nature of a single-crystal SAED pattern,

serving as a magnified projection of the intersection between the Ewald sphere and the crystal's relrods (extended along the thin crystal's normal direction), deviates from an expected parallelogram distribution in diffraction spots. This deviation introduces an approximately 5% error in measurements between the central spot and the surrounding diffraction spots. This notable discrepancy significantly impacts the precise reconstruction of a primitive cell in initial step. As these inaccuracies accumulate through subsequent reduction treatments, there is a risk of incorrectly determining the Niggli cell. Consequently, these challenges undermine the reliability of the entire reconstruction process, rendering the steps inconclusive or unreliable for practical determination of the Bravais lattice.

To accurately determine the Bravais lattice of a precipitate, we propose a novel methodology leveraging the parent lattice as a reference. By accurately establishing the parent Bravais lattice which is often achieved through precise techniques like X-ray diffraction (XRD), we initially index the parent reflections within superimposed SAED patterns. The aim is to align the angle δ, calculated by Eq. (1), with the angle between the parent zone axes. In the case of cubic crystal system, the angle (θ) between two zone axes [u_1 v_1 w_1] and [u_2 v_2 w_2] can be calculated by Eq. (2), devoid of errors when indices are precise, providing a calibration metric for angle δ between the parent RLPs. By exploiting the intrinsic orientation relationship (OR) between the precipitate and parent phases, this calibrated angle facilitates deduction of corresponding angles for precipitate RLPs from the parent lattice. By selecting parallel RLPs from both phases, this methodology effectively mitigates inaccuracies in RLP angles, potentially eliminating their detrimental impact on the reconstruction of the Bravais lattice.

The error in measuring the length of precipitate RLVs can be minimized by utilizing accurate parent RLVs. Specifically, it is crucial that two distinct RLPs are from the same crystal intersect; this implies that a line of diffraction spots in two SAED patterns should share identical indices. When the spacings of parallel planes from the parent and precipitate (d) exhibit an integral multiple relationship, the length of the precipitate RLV can be calibrated using that of the parent. Once the accurate RLVs are established, corrections can be made to the characteristic parallelogram observed in the SAED pattern of the precipitate. Ultimately, the precise RLVs in the RLPs pave the way for reconstructing the genuine Bravais lattice of the precipitate.

$$\cos\theta=\frac{u_1\cdot u_2+v_1\cdot v_2+w_1\cdot w_2}{\sqrt{u_1^2+v_1^2+w_1^2}\cdot\sqrt{u_2^2+v_2^2+w_2^2}} \tag{2}$$

2.2 Defining parallelogram in SAED pattern

In this paper, multiple characteristic parallelograms representing both the parent and the precipitate are typically depicted within a SAED pattern. For clarity in subsequent analyses, we establish a precise definition for a parallelogram. As illustrated in Fig. 1, the black spots in the SAED pattern correspond to reflections within a characteristic parallelogram, highlighted by a brown background. To describe this parallelogram, we define three RLVs denoted as $\boldsymbol{R}_1$, $\boldsymbol{R}_2$, and $\boldsymbol{R}_3$ originating from the central spot. The rotation from $\boldsymbol{R}_1$ to $\boldsymbol{R}_2$ is counterclockwise, and $\boldsymbol{R}_3$ is defined as the sum of $\boldsymbol{R}_1$ and $\boldsymbol{R}_2$. Subsequent figures will illustrate parallelograms based on this defined structure, although the figures will not explicitly mark $\boldsymbol{R}_1$, $\boldsymbol{R}_2$, and $\boldsymbol{R}_3$, or their respective RLV arrows. To minimize the measurement error, the direct measurement of RLV lengths involves averaging a pair of centrosymmetric spots concerning the central spot.

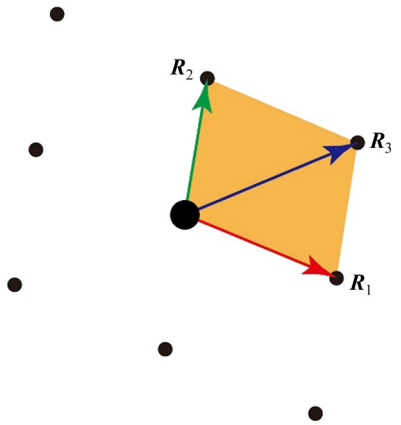

Fig. 1 Schematic diagram illustrating characteristic parallelogram in SAED pattern defined by three vectors $\boldsymbol{R}_1$, $\boldsymbol{R}_2$, and $\boldsymbol{R}_3$

2.3 Materials and characterization

We selected a titanium alloy with a nominal composition of Ti−4.5Al−6.5Mo−2Cr−2Nb−1V−1Sn−1Zr (wt.%). Initially, the alloy underwent a

solution treatment within the single β phase field at 1143 K for 40 min in a vacuum furnace (approximately 133.3 MPa), followed by rapid cooling in argon gas. Subsequently, it was subjected to aging at 653 K for 30 min.

XRD experiments were conducted using a Bruker D8 Advance X-ray diffractometer with Cu K_α radiation at an accelerating voltage of 40 kV and a current of 40 mA. For TEM analysis, specimens were initially sliced, mechanically ground, and shaped into 3 mm discs with an approximate thickness of 80 μm. Further preparation involved dimpling and ion-milling at 5 kV. The TEM analysis was performed using a Talos F200X field emission TEM operating at 200 kV, equipped with a double-tilt holder (±30°). The tilt readings of the double-tilt holder are denoted as A and B in subsequent references.

Additionally, a series of morphology images of the precipitates were obtained using a single-tilt holder, ranging from −66° to +66° with an increment of 1°. The collected tomography data was aligned and reconstructed using Inspect 3D 4.2 and Avizo 9 software.

3 Results and discussion

3.1 Morphology

Figure 2(a) shows a typical morphology of the titanium alloy specimen after solution and aging treatments [22,23]. There are a large number of precipitates with the length of about 500 nm in the parent. A subsequent 3D morphological reconstruction (Fig. 2(b)) reveals that these precipitates possess a plate-like structure, aligned parallel to $\{111\}_\beta$ habit planes. This alignment suggests a potential specific OR with the parent phase, indicating crystallographically equivalent variants likely in multiples of four, given that the $\{111\}_\beta$ in the cubic system comprises four crystal planes. Figure 2(c) presents a dark-field image of the precipitates, obtained by selecting a

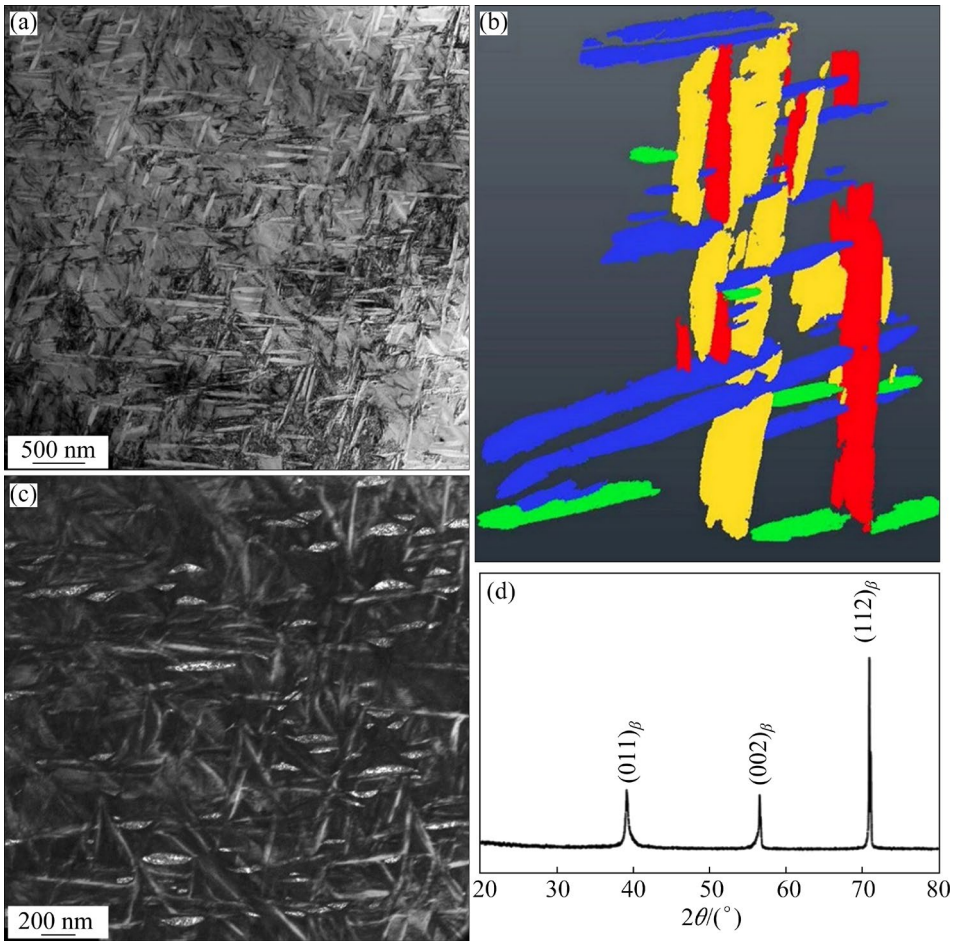

Fig. 2 Bright-field TEM image showing typical morphology of precipitate (a), 3D morphological reconstruction of precipitates (b), dark-field TEM image of some variants in (a), and XRD pattern of solution−aging-treated titanium alloy (d)

single reflection. This image indicates potential overlap of reflections from different variants. Contrarily, the XRD results (Fig. 2(d)) primarily exhibit diffraction peaks from the parent phase, confirming its body-centered cubic (BCC) structure with lattice constant of a_β=0.3254 nm [5]. Notably, the precipitates depicted in Figs. 2(a−c) defy indexing with any known phases, hinting at the possibility of belonging to a novel metastable transition phase within titanium alloys.

3.2 Bravais lattice reconstruction

In Figs. 3(a, b, c), three in situ superimposed SAED patterns are depicted. Within each pattern, strong diffraction spots align to form a distinct parallelogram characteristic of the parent phase.

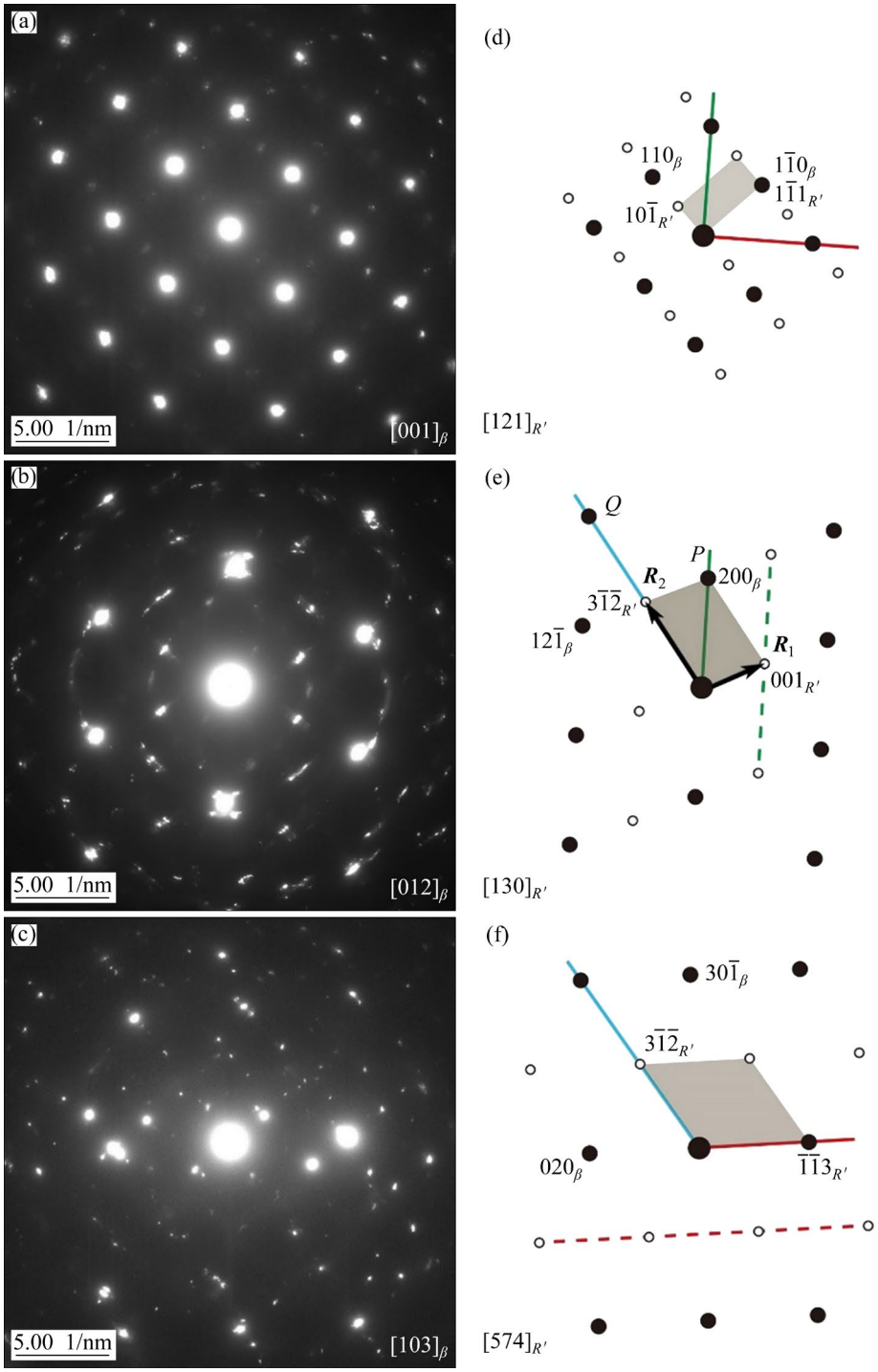

Fig. 3 Three in situ SAED patterns (a−c) and corresponding schematic diagrams showing indexed results of patterns (d−f): (a) A=19.94°, B=−5.42°; (b) A=−5.62°, B=−1.23°; (c) A=22.34°, B=14.94°

However, the weak diffraction spots in these patterns lack a discernible parallelogram structure, suggesting their origin from various precipitates. Figures 3(d, e, f) schematically illustrate the primary distribution of both strong (solid circles) and weak (open circles) diffraction spots observed in Figs. 3(a, b, c), respectively.

Firstly, Figs. 3(d, e, f) denote the indexing of parent reflections. Using the double-tilt holder readings and the parent zone axes, we calculated two angles between RLPs, i.e. δ (obtained from Eq. (1)) and θ (obtained from Eq. (2)). Table S1 and Fig. S1 in Supporting Information show their consistency, with a maximum deviation of only 0.7° in Fig. 3, attributed to errors in tilt holder readings and precisely acquiring on-zone SAED patterns, hence yielding accurate θ angles between RLPs.

Secondly, precise RLV lengths from both strong and weak diffraction spots were calculated. Figures 3(d, e, f) illustrate intersection lines between superimposed RLPs by colored lines, where the lengths of parent and precipitate RLVs along these lines should be equal or integral multiples. For instance, in Fig. 3(e), parent RLVs accurately measured in XRD (Fig. 2(d)) helped determine the lengths of precipitate RLVs along specific intersection lines, allowing precise correction of the precipitate's parallelogram based on the parent lattice parameters. Comparative RLV lengths corrected from SAED patterns are tabulated in Table S2 in Supporting Information.

Finally, the Bravais lattice of the unknown phase (R' phase) was reconstructed. In Section 2.1, we selected basis vectors ($\boldsymbol{a}_0$, $\boldsymbol{b}_0$, $\boldsymbol{c}_0$) for a reciprocal primitive cell. In Figs. 3(d) and (e), parallelograms $\boldsymbol{R}_1$ and $\boldsymbol{R}_2$ were chosen as $\boldsymbol{a}_0$ and $\boldsymbol{b}_0$, respectively. Subsequently, parallelogram $\boldsymbol{R}_1$ in Fig. 3(e) was selected as $\boldsymbol{c}_0$, aiding in determining the lattice parameters of the R' phase: $a_{R'}=b_{R'}=c_{R'}=0.5395$ nm, $\alpha_{R'}=\beta_{R'}=\gamma_{R'}=117.04°$. Once the lattice parameters of R' phase are determined, the weak diffraction spots can be indexed, as shown in Figs. 3(d, e, f).

In this study, we used 10 in situ SAED patterns to systematically analyze crystallographic data, thereby confirming the presence of the rhombohedral R' phase in the titanium alloy.

3.3 OR between R' phase and parent phase

One may argue the hypothesis regarding the existence of parallel relations between the precipitate and the parent phase. Figure 4(a) presents an ex situ superimposed SAED pattern along the $[111]_\beta$ zone axis, accompanied by the corresponding high-resolution TEM image and fast Fourier transform (FFT) results depicted in Fig. 4(b). Observation from Figs. 4(a) and (b) indicates that, along the viewing direction $[111]_\beta$, two crystal planes of the R' phase align parallel to those of the parent phase.

The indexed results, presented in Fig. 4(c), demonstrate the OR between the R' phase and the parent phase, affirming the following relationship:

$$\begin{cases}(001)_{R'}//(1\bar{2}1)_\beta\\(\bar{1}10)_{R'}//(\bar{1}01)_\beta\\[110]_{R'}//[111]_\beta\end{cases} \tag{3}$$

As far as our current knowledge extends, the relationship defined by Eq. (3) has not been previously documented within BCC−rhombohedral systems. Additionally, this relationship can be expressed mathematically in a matrix form:

$$\begin{bmatrix}U\\V\\W\end{bmatrix}_\beta = N\begin{bmatrix}u\\v\\w\end{bmatrix}_{R'} \tag{4}$$

$$\begin{bmatrix}u\\v\\w\end{bmatrix}_{R'} = N^{-1}\begin{bmatrix}U\\V\\W\end{bmatrix}_\beta \tag{5}$$

$$\begin{bmatrix}H\\K\\L\end{bmatrix}_\beta = (N^{\mathrm{T}})^{-1}\begin{bmatrix}h\\k\\l\end{bmatrix}_{R'} \tag{6}$$

$$\begin{bmatrix}h\\k\\l\end{bmatrix}_{R'} = N^{\mathrm{T}}\begin{bmatrix}H\\K\\L\end{bmatrix}_\beta \tag{7}$$

where

$$N=\frac{1}{2}\begin{bmatrix}3&-1&-1\\1&1&-3\\-1&3&-1\end{bmatrix} \tag{8}$$

The lattice parameters of the parent phase and the R' phase have a relationship, i. e., $a_{R'}=\sqrt{11}/2\,a_\beta$ and $a_{R'}=\arccos(-5/11)$ and the following strict parallel relationships can be predicted:

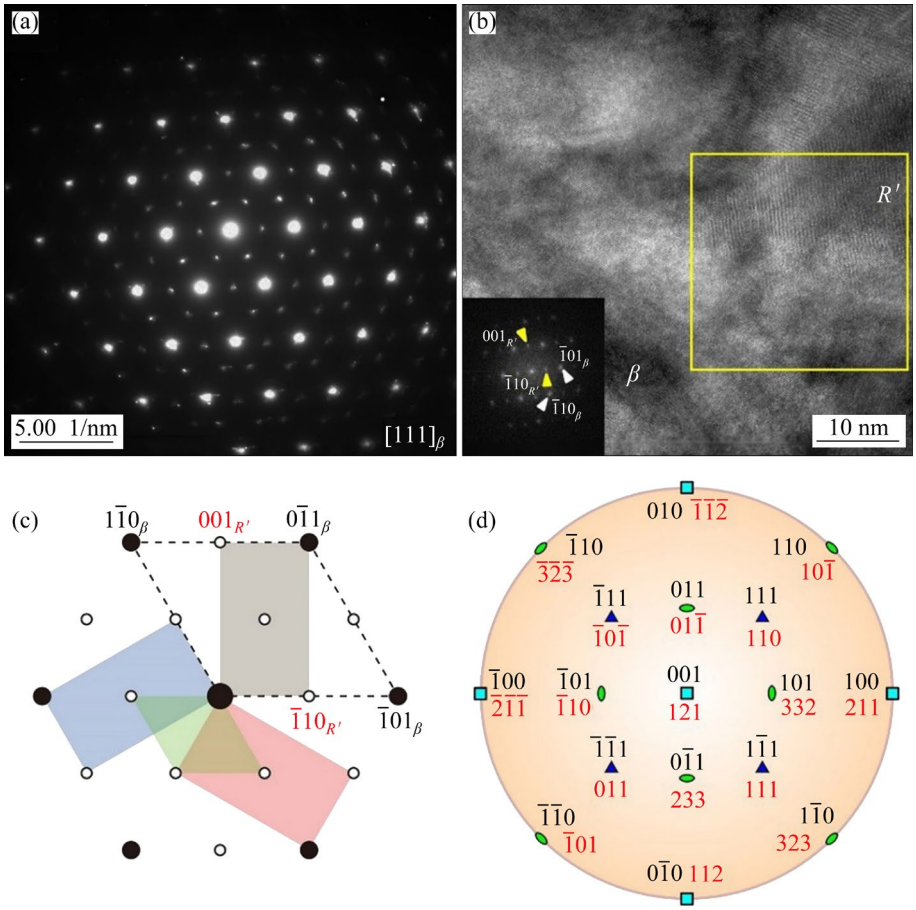

Fig. 4 Superimposed SAED pattern taken along parent $[111]_\beta$ zone axis (a), corresponding high-resolution TEM image and fast Fourier transform (inset) of local region indicated by yellow square (b), indexed results with one dashed line and four colored parallelograms of parent and R' phases, respectively (c), and pole figure with black and red indices corresponding to parent and R' phases, respectively (d)

$$\begin{cases}[121]_{R'}//[001]_\beta \\ [130]_{R'}//[012]_\beta \\ [574]_{R'}//[103]_\beta \end{cases} \tag{9}$$

Equation (9) is in good agreement with the indexed zone axes in Fig. 3, indicating that the RLPs of the precipitate and the parent are exactly parallel to each other.

Although the OR (Eq. (3)) derived from a single parallelogram of the R' phase (highlighted with gray background in Fig. 4(c)) is singular, this OR indicates an expected parallelism between the parent $\langle 111\rangle_\beta$ and four zone axes of the precipitate:

$$\begin{cases}[111]_\beta//[110]_{R'} \\ [11\bar{1}]_\beta//[0\bar{1}\bar{1}]_{R'} \\ [1\bar{1}1]_\beta//[111]_{R'} \\ [\bar{1}11]_\beta//[\bar{1}0\bar{1}]_{R'} \end{cases} \tag{10}$$

As highlighted in Fig. 4(c), the R' reflections along the parent $\langle 111\rangle_\beta$ zone axis exhibit four distinct parallelograms with various background colors, indicating the existence of multiple variants, further elucidated in subsequent sections. Additionally, this OR can be visually represented in a pole figure (Fig. 4(d)), offering a graphical depiction of the crystallographic relationship between the R' phase and the parent phase.

3.4 48 variants of R' phase

In the cubic crystal system, any $\langle u\,v\,w\rangle_\beta$ direction encompasses 48 crystallographically equivalent indices [24]. Consequently, the R' phase, following this OR, is expected to exhibit 48 variants, equally divided between right-handed and left-handed systems. Figure 5 depicts 24 right-handed variants, as the left-handed counterparts mirror the right-handed ones by reversing the basis vector directions. These variants, defined by their four

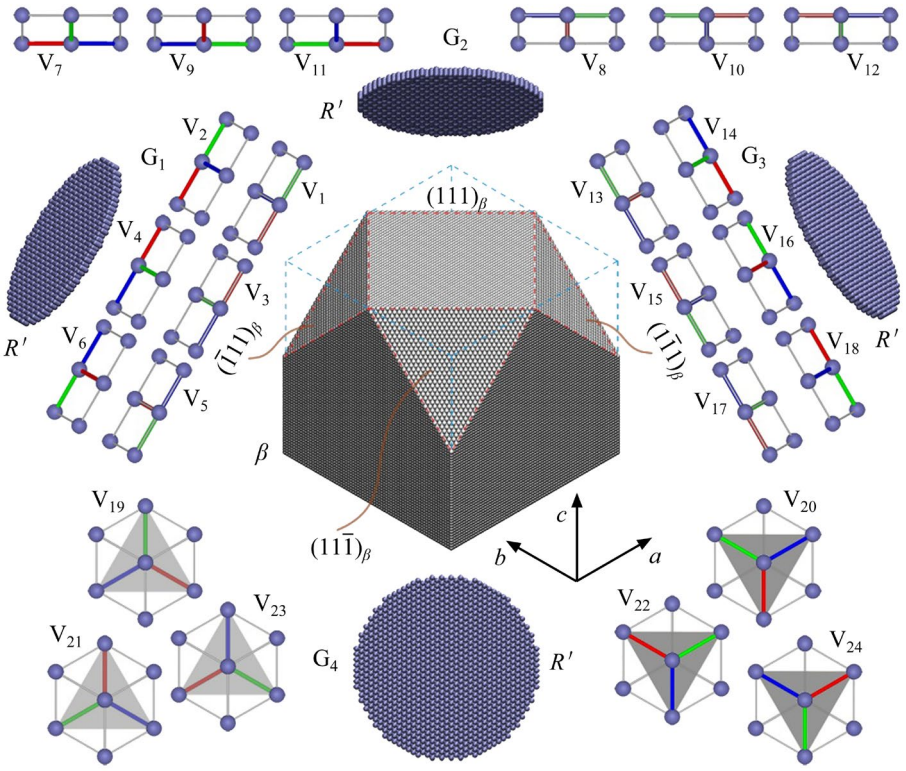

Fig. 5 Variants of R' phase and their geometric configurations in parent phase (Only 24 right-handed variants are displayed, and the remaining 24 left-handed ones are simply those with concurrently reverse basis vector directions of the right-handed ones)

$\{u\,v\,w\}_\beta$ habit planes, are organized into four groups (G_1−G_4), where each group contains 12 variants, i.e. six right-handed and six left-handed, presenting similar appearances but alternating basis vectors. For instance, in Group G_1, Variants 1 and 6 (V_1 and V_6) share a relationship between their basis vectors: $\boldsymbol{a}_6=-\boldsymbol{c}_1$, $\boldsymbol{b}_6=-\boldsymbol{b}_1$, $\boldsymbol{c}_6=-\boldsymbol{a}_1$.

A comprehensive correspondence between the basis vectors of all 24 right-handed variants and those of the BCC parent phase is shown in Table 1.

3.5 Identifying variants in SAED patterns

As all variants have been categorized into four distinct groups (as listed in Table 1), their differentiation and detection within SAED patterns become feasible. To ensure the accuracy of variant indices, it is crucial to consider both the parent reflections and the established OR between the R' phase and the parent phase.

Here, we reindexed Fig. 3 to include all variants, presenting the outcomes in Fig. 6. In this depiction, larger black solid circle signifies the central spot, while smaller black solid circles represent strong parent reflections [25,26]. Additionally, smaller red solid circles indicate weak reflections arising from the R' phase, whereas red open circles signify the locations of reciprocal lattice points from all variants. Each reciprocal lattice point of precipitate is accompanied by up to four colored ellipses, each enclosing a local range of reflections from the R' phase. The four colored parallelograms, defined by the reciprocal lattice points of the R' phase, correspond to Groups G_1−G_4. It is essential to highlight that while certain parallelograms may appear equivalent in one RLP (e.g., G_1 and G_3 in Fig. 6(a)), they differ when observed in other RLPs (e.g., G1 and G3 in Figs. 6(b) and (c)). Furthermore, the major axes of the ellipses align roughly with the projections of various variants' relrods onto each RLP. For instance, in a RLP represented in Fig. 6(b) (also in Fig. 3(e)), the projections of the relrods associated with Groups G_1−G_4 are denoted by four colored rods intersecting the central spot. Notably, the colors of these rods, ellipses, and parallelograms consistently correlate with each other in all figures.

Table 1 Correspondence between basis vectors of 24 right-handed variants and parent

Group	Variant	Basis vector		
		$[100]_{R'}$	$[010]_{R'}$	$[001]_{R'}$
G_1	V_1	$1/2[\bar{3}\,\bar{1}\,\bar{1}]_\beta$	$1/2[1\,\bar{1}\,3]_\beta$	$1/2[1\,3\,\bar{1}]_\beta$
	V_2	$1/2[\bar{1}\,1\,\bar{3}]_\beta$	$1/2[3\,1\,1]_\beta$	$1/2[\bar{1}\,3\,1]_\beta$
	V_3	$1/2[1\,\bar{1}\,3]_\beta$	$1/2[1\,3\,\bar{1}]_\beta$	$1/2[\bar{3}\,\bar{1}\,\bar{1}]_\beta$
	V_4	$1/2[3\,1\,1]_\beta$	$1/2[\bar{1}\,\bar{3}\,1]_\beta$	$1/2[\bar{1}\,1\,\bar{3}]_\beta$
	V_5	$1/2[1\,3\,\bar{1}]_\beta$	$1/2[\bar{3}\,\bar{1}\,\bar{1}]_\beta$	$1/2[1\,\bar{1}\,3]_\beta$
	V_6	$1/2[\bar{1}\,\bar{3}\,1]_\beta$	$1/2[\bar{1}\,1\,\bar{3}]_\beta$	$1/2[3\,1\,1]_\beta$
G_2	V_7	$1/2[\bar{1}\,3\,\bar{1}]_\beta$	$1/2[\bar{1}\,\bar{1}\,3]_\beta$	$1/2[3\,\bar{1}\,\bar{1}]_\beta$
	V_8	$1/2[1\,1\,\bar{3}]_\beta$	$1/2[1\,\bar{3}\,1]_\beta$	$1/2[\bar{3}\,1\,1]_\beta$
	V_9	$1/2[\bar{1}\,\bar{1}\,3]_\beta$	$1/2[3\,\bar{1}\,\bar{1}]_\beta$	$1/2[\bar{1}\,3\,\bar{1}]_\beta$
	V_{10}	$1/2[1\,\bar{3}\,1]_\beta$	$1/2[\bar{3}\,1\,1]_\beta$	$1/2[1\,1\,\bar{3}]_\beta$
	V_{11}	$1/2[3\,\bar{1}\,\bar{1}]_\beta$	$1/2[\bar{1}\,3\,\bar{1}]_\beta$	$1/2[\bar{1}\,\bar{1}\,3]_\beta$
	V_{12}	$1/2[\bar{3}\,1\,1]_\beta$	$1/2[1\,1\,\bar{3}]_\beta$	$1/2[1\,\bar{3}\,1]_\beta$
G_3	V_{13}	$1/2[3\,1\,\bar{1}]_\beta$	$1/2[\bar{1}\,1\,3]_\beta$	$1/2[\bar{1}\,\bar{3}\,\bar{1}]_\beta$
	V_{14}	$1/2[1\,\bar{1}\,\bar{3}]_\beta$	$1/2[\bar{3}\,\bar{1}\,1]_\beta$	$1/2[1\,3\,1]_\beta$
	V_{15}	$1/2[\bar{1}\,1\,3]_\beta$	$1/2[\bar{1}\,\bar{3}\,\bar{1}]_\beta$	$1/2[3\,1\,\bar{1}]_\beta$
	V_{16}	$1/2[\bar{3}\,\bar{1}\,1]_\beta$	$1/2[1\,3\,1]_\beta$	$1/2[1\,\bar{1}\,3]_\beta$
	V_{17}	$1/2[\bar{1}\,\bar{3}\,\bar{1}]_\beta$	$1/2[3\,1\,\bar{1}]_\beta$	$1/2[\bar{1}\,1\,3]_\beta$
	V_{18}	$1/2[1\,3\,1]_\beta$	$1/2[1\,\bar{1}\,\bar{3}]_\beta$	$1/2[\bar{3}\,\bar{1}\,1]_\beta$
G_4	V_{19}	$1/2[1\,\bar{3}\,\bar{1}]_\beta$	$1/2[1\,1\,3]_\beta$	$1/2[\bar{3}\,1\,\bar{1}]_\beta$
	V_{20}	$1/2[\bar{1}\,\bar{1}\,\bar{3}]_\beta$	$1/2[\bar{1}\,3\,1]_\beta$	$1/2[3\,\bar{1}\,1]_\beta$
	V_{21}	$1/2[1\,1\,3]_\beta$	$1/2[\bar{3}\,1\,\bar{1}]_\beta$	$1/2[1\,\bar{3}\,\bar{1}]_\beta$
	V_{22}	$1/2[\bar{1}\,3\,1]_\beta$	$1/2[3\,\bar{1}\,1]_\beta$	$1/2[\bar{1}\,\bar{1}\,\bar{3}]_\beta$
	V_{23}	$1/2[\bar{3}\,1\,\bar{1}]_\beta$	$1/2[1\,\bar{3}\,\bar{1}]_\beta$	$1/2[1\,1\,3]_\beta$
	V_{24}	$1/2[3\,\bar{1}\,1]_\beta$	$1/2[\bar{1}\,\bar{1}\,\bar{3}]_\beta$	$1/2[\bar{1}\,3\,1]_\beta$

The discrepancy observed between the positions of the R' phase reflections (red solid circles) and their corresponding reciprocal lattice points (red open circles) can be attributed to the geometric relationship between relrods and the Ewald sphere, illustrated in Fig. 7. In this depiction, red and blue relrods, originating from a shared reciprocal lattice point S, intersect the Ewald sphere at points M_0 and N_0. These intersections, projected along the diffracted beams, result in visible spots M and N, respectively, within a RLP (Fig. 7(a)). The recorded 2D diffraction pattern (Fig. 7(b)) shows the divergence of reflections M and N from the common point S. Notably, relrods belonging to Groups G_3 and G_4 align with $[1\bar{1}1]_\beta$ and $[11\bar{1}]_\beta$

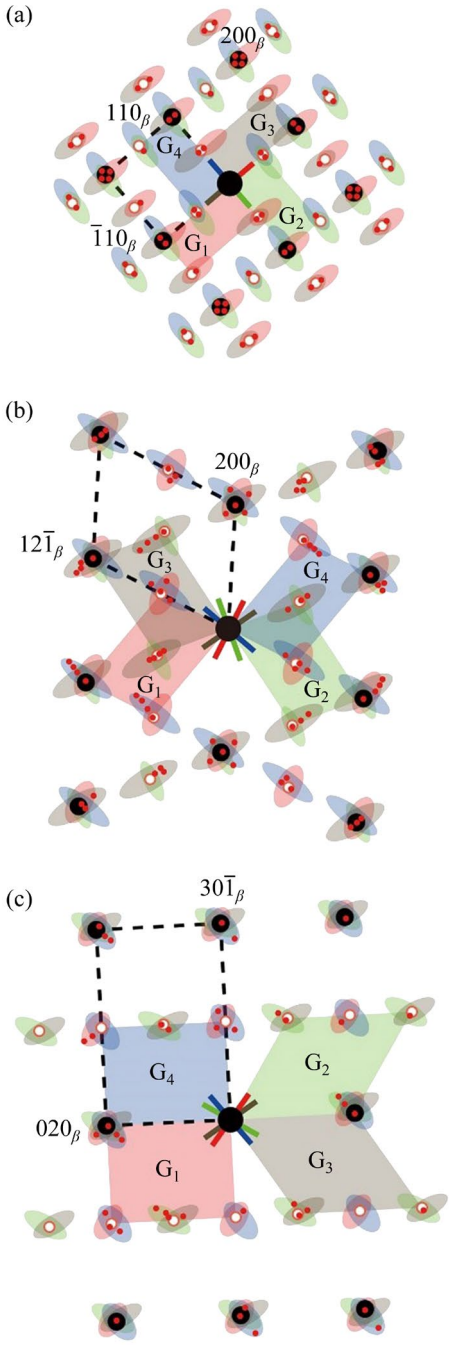

Fig. 6 Schematic diagrams along $[001]_\beta$ (a), $[012]_\beta$ (b), and $[103]_\beta$ (c) zone axes illustrating all four variant groups in SAED patterns shown in Fig. 3

directions, as illustrated in Fig. 5, and precisely coincide with the parent $[011]_\beta$ RLP. Thus, these relrods are directly observable along the viewing direction. Figure 7(c) provides a comprehensive view of the relrods, enabling an estimation of their length, measuring approximately 2.9 nm^{-1}.

The finalized indexing outcomes for the variants are compiled in Tables 2 and 3, which are not directly integrated into the figures for the

enhanced clarity. For a comprehensive understanding of the indexing process and the geometric interplay between relrods and Ewald sphere, detailed information is available in Section 2 in Supporting Information. Table 2 presents the indices of one representative variant (one of the six right-handed variants) from each group. Meanwhile, Table 3 presents the interrelations among indices in each

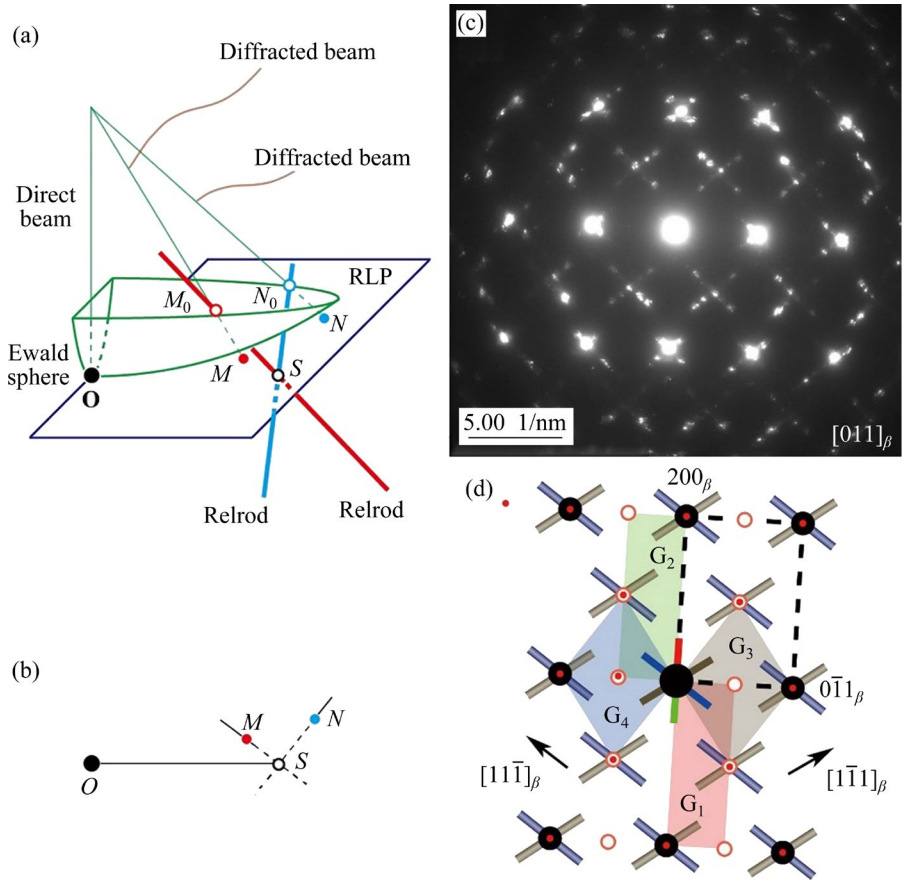

Fig. 7 3D (a) and 2D (b) schematic diagrams showing geometric relationship between relrods and Ewald sphere, in situ SAED pattern along $[011]_\beta$ zone axis, with two sets of directly visible relrods along $[1\bar{1}1]_\beta$ and $[11\bar{1}]_\beta$ directions (c), and parent indexed results and colored parallelograms of G_1−G_4 (d)

Table 2 Summary of indexed results of first variant for G_1−G_4 in in situ SAED patterns ($\boldsymbol{R_1}$ and $\boldsymbol{R_2}$ are two RLVs defining parallelogram as illustrated in Fig. 1)

Figure No.	G_1		G_2		G_3		G_4	
	$\boldsymbol{R}_1$	$\boldsymbol{R}_2$	$\boldsymbol{R}_1$	$\boldsymbol{R}_2$	$\boldsymbol{R}_1$	$\boldsymbol{R}_2$	$\boldsymbol{R}_1$	$\boldsymbol{R}_2$
Fig. 6(a)	$(1\,\bar{1}\,1)$	$(10\,\bar{1})$	$(\bar{1}1\,\bar{1})$	$(\bar{1}01)$	$(1\,\bar{1}1)$	$(10\,\bar{1})$	$(\bar{1}1\,\bar{1})$	$(\bar{1}01)$
Fig. 6(b)	$(\bar{1}\,\bar{1}2)$	$(2\bar{2}1)$	$(\bar{1}2\bar{2})$	$(\bar{2}11)$	$(3\,\bar{1}\,\bar{2})$	$(00\,\bar{1})$	(100)	$(21\bar{3})$
Fig. 6(c)	$(\bar{1}\,\bar{1}3)$	$(20\,\bar{1})$	$(\bar{3}11)$	$(\bar{2}\,\bar{1}3)$	$(\bar{3}12)$	$(\bar{1}\,\bar{1}3)$	$(10\bar{2})$	$(\bar{3}11)$
Fig. 7(d)	$(3\,\bar{1}\,\bar{1})$	$(01\,\bar{1})$	$(\bar{1}\,\bar{1}3)$	$(1\,\bar{1}0)$	$(\bar{2}11)$	(100)	$(00\,\bar{1})$	$(\bar{1}\,\bar{1}2)$
Fig. 8(c)	$(\bar{1}01)$	$(1\bar{3}3)$	$(\bar{1}1\,\bar{1})$	$(\bar{2}11)$	$(00\,\bar{1})$	$(\bar{1}01)$	$(11\bar{2})$	$(\bar{1}1\,\bar{1})$
Fig. 8(d)	$(5\,\bar{1}\,\bar{3})$	$(01\,\bar{1})$	$(\bar{1}10)$	$(\bar{1}02)$	$(1\,\bar{1}\,\bar{1})$	$(\bar{2}01)$	$(01\bar{2})$	$(\bar{1}\,\bar{1}1)$
Fig. 9(b)	$(3\,\bar{1}\,\bar{2})$	$(11\bar{3})$	$(\bar{1}02)$	$(3\,\bar{1}\,\bar{1})$	$(11\bar{3})$	$(\bar{2}01)$	$(3\,\bar{1}\,\bar{1})$	$(21\bar{3})$
Fig. S2(c)	$(20\,\bar{1})$	$(11\bar{2})$	$(\bar{3}3\,\bar{1})$	$(\bar{1}01)$	$(2\,\bar{1}\,\bar{1})$	$(10\bar{2})$	$(10\,\bar{1})$	$(00\,\bar{1})$
Fig. S2(d)	$(01\,\bar{1})$	$(\bar{2}10)$	$(13\bar{5})$	$(\bar{1}10)$	$(2\,\bar{1}0)$	$(1\,\bar{1}\,\bar{1})$	$(\bar{1}\,\bar{1}1)$	$(\bar{1}02)$
Fig. S3(b)	$(\bar{1}\,\bar{1}3)$	(100)	$(\bar{3}11)$	$(\bar{1}\,\bar{1}2)$	$(\bar{2}11)$	$(\bar{1}\,\bar{1}3)$	$(00\,\bar{1})$	$(\bar{3}11)$

Table 3 Relationship of Miller indices among six right-handed variants within each group (G_1−G_4) (($h_1k_1l_1$) and ($h_2k_2l_2$) are the first variant indices of reflections corresponding to $\boldsymbol{R}_1$ and $\boldsymbol{R}_2$ defined in Fig. 1, respectively)

Group	Variant	Reciprocal lattice vector	
		$\boldsymbol{R}_1$	$\boldsymbol{R}_2$
G_1	V_1	$(h_1k_1l_1)$	$(h_2k_2l_2)$
	V_2	$(\bar{k}_1\bar{h}_1\bar{l}_1)$	$(\bar{k}_2\bar{h}_2\bar{l}_2)$
	V_3	$(k_1l_1h_1)$	$(k_2l_2h_2)$
	V_4	$(\bar{h}_1\bar{l}_1\bar{k}_1)$	$(\bar{h}_2\bar{l}_2\bar{k}_2)$
	V_5	$(l_1h_1k_1)$	$(l_2h_2k_2)$
	V_6	$(\bar{l}_1\bar{k}_1\bar{h}_1)$	$(\bar{l}_2\bar{k}_2\bar{h}_2)$
G_2	V_7	$(h_1k_1l_1)$	$(h_2k_2l_2)$
	V_8	$(\bar{k}_1\bar{h}_1\bar{l}_1)$	$(\bar{k}_2\bar{h}_2\bar{l}_2)$
	V_9	$(k_1l_1h_1)$	$(k_2l_2h_2)$
	V_{10}	$(\bar{h}_1\bar{l}_1\bar{k}_1)$	$(\bar{h}_2\bar{l}_2\bar{k}_2)$
	V_{11}	$(l_1h_1k_1)$	$(l_2h_2k_2)$
	V_{12}	$(\bar{l}_1\bar{k}_1\bar{h}_1)$	$(\bar{l}_2\bar{k}_2\bar{h}_2)$
G_3	V_{13}	$(h_1k_1l_1)$	$(h_2k_2l_2)$
	V_{14}	$(\bar{k}_1\bar{h}_1\bar{l}_1)$	$(\bar{k}_2\bar{h}_2\bar{l}_2)$
	V_{15}	$(k_1l_1h_1)$	$(k_2l_2h_2)$
	V_{16}	$(\bar{h}_1\bar{l}_1\bar{k}_1)$	$(\bar{h}_2\bar{l}_2\bar{k}_2)$
	V_{17}	$(l_1h_1k_1)$	$(l_2h_2k_2)$
	V_{18}	$(\bar{l}_1\bar{k}_1\bar{h}_1)$	$(\bar{l}_2\bar{k}_2\bar{h}_2)$
G_4	V_{19}	$(h_1k_1l_1)$	$(h_2k_2l_2)$
	V_{20}	$(\bar{k}_1\bar{h}_1\bar{l}_1)$	$(\bar{k}_2\bar{h}_2\bar{l}_2)$
	V_{21}	$(k_1l_1h_1)$	$(k_2l_2h_2)$
	V_{22}	$(\bar{h}_1\bar{l}_1\bar{k}_1)$	$(\bar{h}_2\bar{l}_2\bar{k}_2)$
	V_{23}	$(l_1h_1k_1)$	$(l_2h_2k_2)$
	V_{24}	$(\bar{l}_1\bar{k}_1\bar{h}_1)$	$(\bar{l}_2\bar{k}_2\bar{h}_2)$

group, elucidating their association with a specific-colored parallelogram. The evaluation criteria for the indexed results are as follows: (1) Consistency of angles between parent RLPs, i.e., δ and θ, particularly crucial in in situ acquired SAED patterns. In 10 in situ SAED patterns, the maximum and average deviations between δ and θ are recorded as 5.13° and 1.36°, respectively, and the details are listed in Table S1 in Supporting Information. (2) Consistency between the zone axes of the same variant and that of the parent phase. For instance, considering Table 2, the zone axis of Variant V_1 in Fig. 6(a) is $[121]_{V_1}$, and that in Fig. 7(d) is $[233]_{V_1}$. The calculated angle between these zone axes (45.01°) aligns well with the angle (45.00°) derived from the parent zone axes (Table S1 in Supporting Information). (3) Uniqueness of intersection lines between different RLPs, whether defined by common RLVs from the parent or any variant. For example, in Figs. 6(a) and 7(d), the reflection between two parent RLPs is $(200)_\beta$, whereas the common reflection of Variant V_{13} in both RLPs is the same $(3\bar{1}\bar{1})_{V_{13}}$, as anticipated.

3.6 Understanding of complicated SAED patterns of variants

The zero-order reflections among different variants tend to overlap within the same group and even across different groups, adding complexity to the SAED patterns of precipitates. For illustration, two SAED patterns along $[\bar{1}13]_\beta$ and $[\bar{1}33]_\beta$ zone axes displaying zero- and 1st-order reflections are shown in Figs. 8(a) and (b), respectively. The corresponding indexing procedures are depicted in Figs. 8(c−f). In Figs. 8(c) and (d), only the reciprocal lattice points calculated from the reconstructed structure and the established OR are visible. The black solid circles and red open circles represent zero-order reflections from the parent and the variants, respectively. Meanwhile, the green open circles denote the projected positions of the 1st-order reflections from the variants. Solid and dash-dotted lines outline parallelograms of 1st-order reciprocal lattice points from right-handed and left-handed variants, respectively. Moving to Figs. 8(e) and (f), the green solid circles mark 1st-order reflections from the variants. Enclosed by solid and dash-dotted lines, the open ellipses cover local ranges of the 1st-order reflections from right-handed and left-handed variants, respectively. All symbols and their colors in Fig. 8 align consistently with those in Fig. 6.

Indexed results for zero-order reflections of the variants are presented in Tables 2 and 3. Notably, the analysis of the 1st-order reflections reveals intriguing aspects. For instance, in Fig. 8(c), the parallelogram of G_3 exhibits a layer-spacing of 1.8534 nm^{-1}, rendering it unable to produce the 1st-order reflections. Conversely, G_1, G_2, and G_4, with identical areas and a layer-spacing of 0.9267 nm^{-1}, display distinct 1st-order reflections, as evident in Fig. 8(e). Similarly, in Figs. 8(d) and

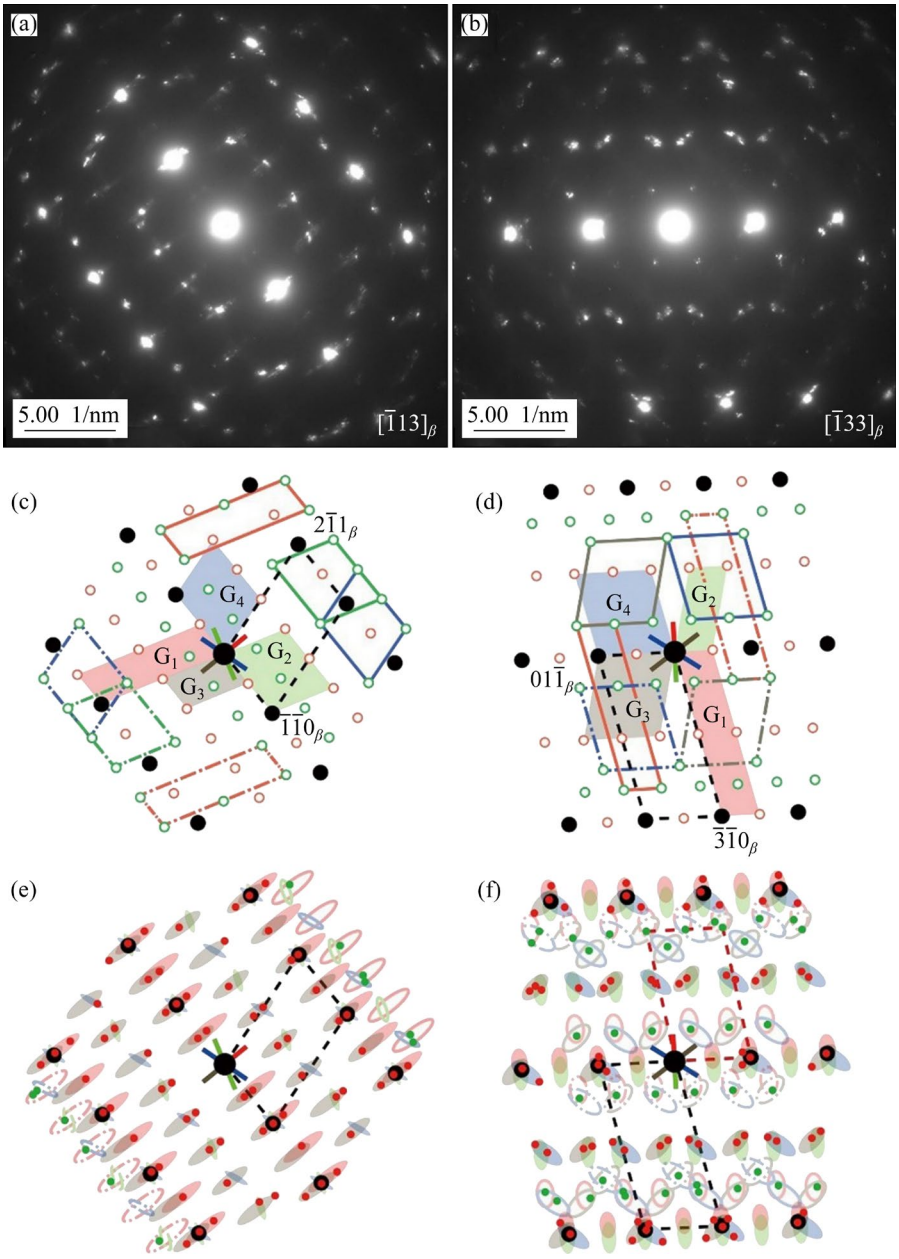

Fig. 8 Two in situ superimposed SAED patterns with zero- and 1st-order reflections: (a) $[\bar{1}13]_\beta$ zone axis with A=0.59° and B=−20.03°; (b) $[\bar{1}33]_\beta$ zone axis with A=−26.28° and B=−14.85°; (c, d) and (e, f) Schematic diagrams showing indexing processes and indexed results for (a) and (b), respectively

(f), only G_1, G_3, and G_4, characterized by a 0.7051 nm^{-1} layer-spacing, present the 1st-order reflections. A discernible contrast between Figs. 8(e) and (f) lies in the presence of the 1st-order reflections near the central spot, attributed to differences in layer-spacing (0.7051 nm^{-1} vs 0.9267 nm^{-1}). Further indexed results of in situ superimposed SAED patterns featuring higher-order reflections are available in Section 3 in Supporting Information.

As the RLP layer-spacing decreases, all 48 variants can display the 1st-order reflections (Fig. S3 in Supporting Information), and in some cases, even the 2nd-order reflections may emerge, as depicted in Fig. 9. The complex SAED pattern (Fig. 9(a)) comprises zero-, 1st-, and 2nd-order reflections from the 48 variants alongside the parent reflections. Figure 9(b) highlights reciprocal lattice points of both the variants and the parent along $[\bar{1}03]_\beta$ zone axis. Leveraging the R' phase lattice parameters (Section 3.2) and its OR with the parent (Section 3.3), the zero-order parallelograms

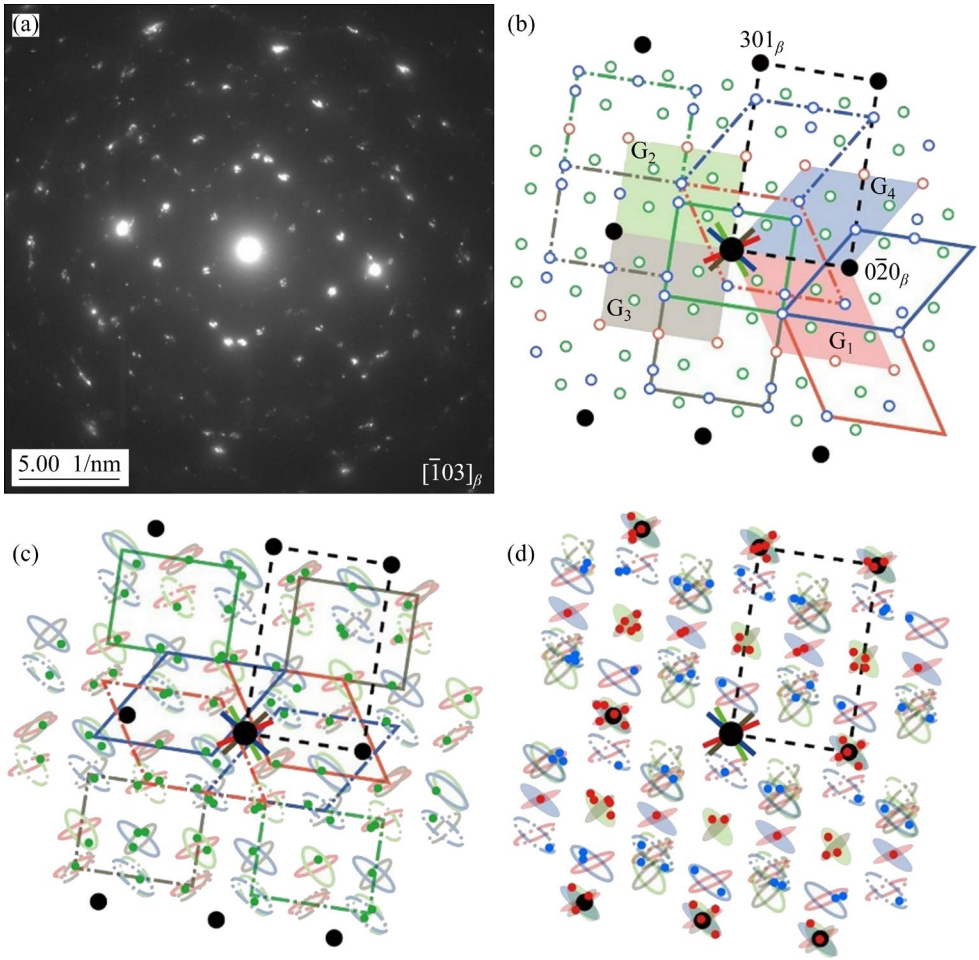

Fig. 9 In situ superimposed SAED pattern along $[\bar{1}03]_\beta$ zone axis with A=17.00° and B=−24.23° (a), and corresponding schematic indexing processes (b−d) (The solid and dash-dotted lines in (b) define 2nd-order parallelograms of right-handed and left-handed variants, respectively, and those in (c) represent 1st-order ones)

of G_1−G_4 are distinguished and indexed (refer to Fig. 9(b) and Tables 2 and 3). In this scenario, the RLP layer-spacing for G_1−G_4 is 0.4859 nm^{-1} (considerably less than the relrod half-length of 1.45 nm^{-1}), which accounts for the discrete arrangement of high-order reflections around the reciprocal lattice points. Figure 9(c) and (d) specifically illustrate the 1st- and 2nd-order reflections of the variants.

Finally, we emphasize that the numerous variants and the high-order reflections significantly increase the complexity of the SAED patterns, and therefore indexing such a pattern can be challenging and sometimes erroneous. As an example, in Fig. 8(f), the red dashed lines enclose a parallelogram defined by both zero- and 1st-order reflections, seemingly suggestive of indexing as the R' phase. However, this definition does not align the RLP with that of the parent, leading to erroneous crystallographic conclusions. Therefore, the criteria outlined in Section 3.5 are strongly advised to ensure the accuracy and validity of the indexed results. Further analysis of high-order reflections becomes instrumental not only in confirming the reconstructed Bravais lattice of the new phase but also in classifying its 48 variants.

4 Conclusions

(1) The identification of a novel rhombohedral R' phase in a titanium alloy (Ti−4.5Al−6.5Mo−2Cr−2Nb−1V−1Sn−1Zr, wt.%) following specific thermal treatments (solution: 1143 K, 40 min; aging: 653 K, 30 min) marks a significant advancement in materials science. We introduce an accurate methodology reliant on a limited set of three SAED patterns for the reconstruction of the Bravais lattice within such unknown precipitates.

(2) The R' phase manifests a distinct rhombohedral lattice, characterized by specific

parameters ($a=b=c$=0.5395 nm, $\alpha=\beta=\gamma$=117.04°). Our analysis further reveals a definitive relationship between the lattice parameters of the R' phase and the body-centered cubic (BCC) parent phase, facilitating a deeper understanding of their structural interplay ($a_{R'}=\sqrt{11}/2a$, a_R=arccos(−5/11).

(3) Crucially, our study delineates the OR between the R' phase and the parent phase. Additionally, it categorizes the R' phase into 48 variants across four distinct groups, each comprising 12 variants characterized by differing handedness in their basis vectors.

(4) Through the in situ acquisition and meticulous indexing of SAED patterns from all 48 variants, supplemented by a detailed examination of high-order reflections, our findings validate the identified lattice parameters of the R' phase and its OR with the parent phase. Furthermore, we propose key criteria for assessing the accuracy of indexed results, offering pivotal insights into the theoretical underpinnings governing titanium alloys.

(5) Overall, this study not only delineates the structural characteristics of the newly discovered R' phase but also introduces a robust methodology for precise lattice reconstruction within unknown precipitates. These insights hold significant promise for advancing the understanding and application of titanium alloys within the broader materials science landscape.

CRediT authorship contribution statement

Xin-nan WANG: Investigation, Methodology, Conceptualization, Experiment, Data curation, Writing − Original draft; **Ming HAN:** Supervision, Writing − Review & editing; **Fu-rong ZHANG:** Writing − Review & editing; **Guang-ming ZHAO:** Data curation, Writing − Review & editing; **Zhi-shou ZHU:** Funding acquisition, Supervision, Resources, Writing − Review & editing.

Declaration of competing interest

The authors declare that they have no known competing financial interests or personal relationships that could have appeared to influence the work reported in this paper.

Acknowledgments

The authors acknowledge financial supports from the National Natural Science Foundation of China (No. 51071125), and the Major Project of Department of Education of Jiangxi Province, China (No. GJJ210605).

Supporting Information

Supporting Information in this paper can be found at: http://tnmsc.csu.edu.cn/download/09-p2849-2023-0304-Supporting_Information.pdf.

References

[1] BUENCONSEJO P J S, KIM H Y, MIYAZAKI S. Effect of ternary alloying elements on the shape memory behavior of Ti−Ta alloys [J]. Acta Materialia, 2009, 57: 2509−2515.

[2] LI Q, NIINOMI M, HIEDA J, NAKAI M, CHO K. Deformation-induced ω phase in modified Ti−29Nb−13Ta−4.6Zr alloy by Cr addition [J]. Acta Biomaterialia, 2013, 9: 8027−8035.

[3] YANG Chao, LI Miao-quan, LIU Yin-gang. Severe plastic deformation induced precipitation of the ordered α-Ti_3Al phase in Ti−5Al−2Sn−2Zr−4Mo−4Cr [J]. Journal of Alloys and Compounds, 2021, 854: 157277−157286.

[4] ZHOU Zhong-bo, FEI Yue, LAI Min-jie, KOU Hong-chao, CHANG Hui, SHANG Guo-qiang, ZHU Zhi-shou, LI Jin-shan, ZHOU Lian. Microstructure and mechanical properties of new metastable β type titanium alloy [J]. Transactions of Nonferrous Metals Society of China, 2010, 20: 2253−2258.

[5] ZHANG Yang, XIANG Song, TAN Yuan-biao, JI Xuan-ming. Study on ω-assisted α nucleation behavior of metastable β-Ti alloys from phase transformation mechanism [J]. Journal of Alloys and Compounds, 2022, 890: 161686−161694.

[6] HUANG Ze-wen. Ordered ω phases in a 4Zr−4Nb-containing TiAl-based alloy [J]. Acta Materialia, 2008, 56: 1689−1700.

[7] DONG Rui-feng, LI Jin-shan, KOU Hong-chao, FAN Jiang-kun, ZHAO Yu-hong, HOU Hua, WU Li. ω-assisted refinement of α phase and its effect on the tensile properties of a near β titanium alloy [J]. Journal of Materials Science & Technology, 2022, 44: 24−30.

[8] LI Tong, KENT D, SHA Gang, LIU Hong-wei, FRIES S G, CEGUERRA A V, DARGUSCH M S, CAIRNEY J M. Nucleation driving force for ω-assisted formation of α and associated ω morphology in β-Ti alloys [J]. Scripta Materialia, 2018, 155: 149−154.

[9] NAG S, BANERJEE R, SRINIVASAN R, HWANG J Y, HARPER M, FRASER H L. ω-assisted nucleation and growth of α precipitates in the Ti−5Al−5Mo−5V−3Cr−0.5Fe β titanium alloy [J]. Acta Materialia, 2009, 57: 2136−2147.

[10] TANE M, HAGIHARA K, UEDA M, NAKANO T, OKUDA Y. Elastic-modulus enhancement during room-temperature aging and its suppression in metastable Ti−Nb-based alloys with low body-centered cubic phase stability [J]. Acta Materialia, 2016, 102: 373−384.

[11] BENDERSKY L A, BOETTINGER W J, BURTON B P, BIANCANILLO F S, SHOEMAKER C B. The formation of ordered ω-related phases in alloys of composition Ti_4Al_3Nb [J]. Acta Metallurgica et Materialia, 1990, 38: 931−943.

[12] ZHENG Y F, ALAM T, BANERJEE R, BANERJEE D, FRASER H L. The influence of aluminum and oxygen additions on intrinsic structural instabilities in titanium−molybdenum alloys [J]. Scripta Materialia, 2018, 152:

150−153.
[13] LI Tong, LAI Ming-jie, KOSTKA A, SALOMON S, ZHANG Si-yuan, SOMSEN C, DARGUSCH M S, KENT D. Composition of the nanosized orthorhombic *O′* phase and its direct transformation to fine *α* during ageing in metastable *β*-Ti alloys [J]. Scripta Materialia, 2019, 170: 183−188.
[14] ZHENG Yu-feng, WILLIAMS R E A, FRASER H L. Characterization of a previously unidentified ordered orthorhombic metastable phase in Ti−5Al−5Mo−5V−3Cr [J]. Scripta Materialia, 2016, 113: 202−205.
[15] DONG Rui-feng, LI Jin-shan, KOU Hong-chao, FAN Jiang-kun, TANG B. Dependence of mechanical properties on the microstructure characteristics of a near *β* titanium alloy Ti-7333 [J]. Journal of Materials Science & Technology, 2019, 35: 48−54.
[16] ZHENG Yu-feng, WILLIAMS R E A, SOSA J M, ALAM T, WANG Yun-zhi, BANERJEE R, FRASER H L. The indirect influence of the *ω* phase on the degree of refinement of distributions of the *α* phase in metastable *β*-Titanium alloys [J]. Acta Materialia, 2016, 103: 165−173.
[17] NOVOSELOVA T, MALINOV S, SHA W, ZHECHEVA A. High-temperature synchrotron X-ray diffraction study of phases in a gamma TiAl alloy [J]. Materials Science and Engineering A, 2004, 371: 103−112.
[18] DAVID B W, CARTER C B. Transmission electron microscopy: A textbook for materials science [M]. 2nd ed. New York: Springer, 2009.
[19] DEVARAJ A, NAG S, SRINIVASAN R, WILLIAMS R E A, BANERJEE S, BANERJEE R, FRASER H L. Experimental evidence of concurrent compositional and structural instabilities leading to *ω* precipitation in titanium−molybdenum alloys [J]. Acta Materialia, 2012, 60: 596−609.
[20] LAI Ming-jie, TASAN C C, RAABE D. Deformation mechanism of *ω*-enriched Ti−Nb-based gum metal: dislocation channeling and deformation induced *ω*−*β* transformation [J]. Acta Materialia, 2015, 100: 290−300.
[21] NG H P, DEVARAJ A, NAG S, BETTLES C J, GIBSON M, FRASER H L, MUDDLE B C, BANERJEE R. Phase separation and formation of omega phase in the beta matrix of a Ti−V−Cu alloy [J]. Acta Materialia, 2011, 59: 2981−2991.
[22] HUANG Liang, LI Chang-min, LI Cheng-lin, HUI Song-xiao, YU Yang, ZHAO Ming-jie, GUO Shi-qi, LI Jian-jun. Research progress on microstructure evolution and hot processing maps of high strength *β* titanium alloys during hot deformation [J]. Transactions of Nonferrous Metals Society of China, 2022, 32(12): 3835−3859.
[23] LI Xing, WANG Xin-nan, LIU Ke, CAO Guang-hui, LI Ming-bing, ZHU Zhi-shou, WU Su-jun. Hierarchical structure and deformation behavior of a novel multicomponent *β* titanium alloy with ultrahigh strength [J]. Journal of Materials Science & Technology, 2022, 17: 227−242.
[24] ZHANG Ming-xing, KELLY P M. Crystallographic features of phase transformations in solids [J]. Progress in Materials Science, 2009, 54(8): 1101−1170.
[25] SONG Bo, XIAO Wen-long, WANG Jun-shuai, MA Chao-li, ZHOU Lian. Effects of cryogenic treatments on phase transformations, microstructure and mechanical properties of near *β*-Ti alloy [J]. Journal of Alloys and Compounds, 2021, 878: 160495.
[26] LI Xing, WANG Xin-nan, LIU Ke, WANG Jia-yu, GUO Xuan, LI Ming-bing, ZHU Zhi-shou, WU Su-jun. Microstructure evolution and mechanical property of a new multi-component *β* titanium alloy with ultrahigh strength above 1350 MPa [J]. Journal of Materials Research and Technology, 2022, 21: 4860−4875.

β 钛合金中一种新的菱面体相及其 48 种变体

王新南[1]，韩 明[2]，张福荣[2]，赵光明[2]，朱知寿[1]

1. 中国航发北京航空材料研究院 先进钛合金重点实验室，北京 100095；
2. 华东交通大学 材料科学与工程学院，南昌 330013

摘 要：在经固溶时效处理的钛合金(Ti−4.5Al−6.5Mo−2Cr−2Nb−1V−1Sn−1Zr, 质量分数，%)中发现了一种新的菱形相(*R′*)。采用基于传统选区电子衍射(SAED)技术的新型单胞重构方法确定了其精确的 Bravais 晶格参数。揭示了菱形相与 BCC 相之间的取向关系。结果表明，*R′*相有 48 个晶体学等效变体，导致具有高阶反射、复杂的 SAED 花样图。在低指数和高指数带轴上采集一系列原位 SAED 图，48 种变体产生的所有弱反射和强反射都得到了合理的解释，并直接标定了对应的 Miller 指数，证实了菱形相的存在。此外，还提出了一些评价标定结果的标准，这些标准与 Bravais 晶格重构方法相结合能使合金中未知相的微观结构表征得更加清楚。

关键词：钛合金；菱形相；Bravais 晶格重构；变体；取向关系

(Edited by Wei-ping CHEN)